INTERNATIONAL JOURNAL FOR NUMERICAL METHODS IN FLUIDS, VOL. 15, 147–173 (1992)

A NUMERICAL STUDY OF THE LAMINAR INCOMPRESSIBLE FLOW OVER A 6:1 PROLATE SPHEROID AT 10° INCIDENCE

MOSHE ROSENFELD,* MICHA WOLFSHTEIN AND MOSHE ISRAELI

Technion—Israel Institute of Technology, Haifa 32000, Israel

SUMMARY

The steady incompressible laminar flow field over a 6:1 prolate spheroid at 10° incidence and a Reynolds number of $1{\cdot}6 \times 10^6$ is investigated numerically by solving a reduced set of the Navier–Stokes equations. The present study moves one step beyond the boundary layer approximation by relaxing the requirement of an imposed pressure field to permit the calculation of both attached and longitudinal vortical flow fields. The results shed light on the flow properties over slender bodies at intermediate incidence. The longitudinal vortex is found to be weak relative to vortex-dominated flows. Nevertheless, it has pronounced effects on the flow near the surface and on global features of the flow field. A displacement velocity which describes the effect of the vortical flow on the outer inviscid flow is defined. The line on the spheroid where the displacement velocity vanishes closely follows the projection of the vortex centreline on the surface of the spheroid. It is demonstrated numerically that the convergence of the skin friction lines is not a unique criterion for identifying a vortex flow.

KEY WORDS Vortical flow Three-dimensional incompressible flow Prolate spheroid Three-dimensional separation.

1. INTRODUCTION

1.1. Fluid flow over slender bodies

The present work studies the steady incompressible flow field over a 6:1 prolate spheroid at intermediate incidence. The structure of the flow over a blunt slender body depends on several parameters such as the geometry, incidence, Reynolds and Mach numbers, yet the global qualitative characteristics of the flow appear to be similar over a wide range of parameters.

At very low incidence the viscous effects are confined to a thin three-dimensional boundary layer attached to the body. At higher angles of attack (5°–10°) the flow is characterized by three domains.[1] On the windward side, an attached three-dimensional boundary layer is formed. On the leeward side the boundary layer detaches from the body because of the adverse circumferential pressure gradient and rolls up into a pair of longitudinal symmetrical vortices. The effects of these detached vortices on the aerodynamic properties may be significant. At the rear part of the body a domain of separated flow exists with regions of reversed axial velocity. At higher incidence the intensity of the vortices increases and additional pairs of symmetrical

* Present address: Faculty of Engineering, Tel Aviv University, Tel Aviv 69978, Israel.

0271–2091/92/140147–27$18.50

Received December 1989
Revised November 1991

vortices are generated. At a very high incidence (usually above 45°) the symmetry of the flow field breaks up.

The identification of separated flow regions and separation lines is of fundamental importance. In two-dimensional flows the separation point can be easily located because the skin friction vanishes there. In three-dimensional flows the skin friction does not vanish along the entire separation line and may even become larger than in neighbouring regions. Moreover, the addition of the third dimension permits a vast variety of possible structures of the separated flow regions.

Skin friction lines are very valuable in the theoretical analysis of three-dimensional flow separation. A relatively large database of patterns of skin friction lines over aerodynamic bodies has been obtained experimentally by oil streak techniques. Many studies have focused on the relationship between flow separation and the pattern of the skin friction lines using well known topological rules (see e.g. References 2–7).

Tobak and Peake[2] observed that a necessary but not sufficient condition for separation of the flow is the convergence of many skin friction lines into a particular line—the 'separation line'. However, there is still debate on the topological characteristics of separation lines, in particular whether they necessarily emanate from a singular point.[3] Even less clear is the structure of three-dimensional separated flow fields. In two-dimensional flows the separation of the flow leads inevitably to regions of reverse flow in the main direction. In three-dimensional flows the reversal of a velocity component in any direction does not necessarily mean separation of the flow.

To make the problem tractable, many existing experimental and computational studies rely on analysis of the two-dimensional flow near the body to study the three-dimensional flow. However, it is clear that three-dimensional separation is a global phenomenon which requires a comprehensive examination of the complete flow field.[7] A simple criterion for identifying three-dimensional separated regions merely from the skin friction lines cannot be found.

1.2. Experimental data

Experimental results for three-dimensional incompressible flows over slender bodies are scarce. Most of the available studies use the prolate spheroid as a test configuration. Han and Patel[1] visualized the three-dimensional flow field over a spheroid of axial ratio 4·3:1 at several angles of attack and at a low Reynolds number (8×10^4) by injecting dye in a water tunnel. The results are not of sufficient detail and only the gross features of the flow field are described, without quantitative distribution of the flow variables. A principal source of experimental results for incompressible flows over slender bodies was provided by Kreplin *et al.*,[8] who performed a series of experiments to measure the skin friction distribution on a 6:1 prolate spheroid at several angles of attack and Reynolds numbers. In a few cases the pressure distribution was obtained as well. Velocity profiles were measured for a few locations in fully turbulent regions only.

The existence of an experimental database for the incompressible flow over a prolate spheroid, combined with a known potential flow field solution, made this a popular test case for numerical studies of three-dimensional, incompressible and external flows.

1.3. Numerical modelling

Numerical solutions may produce fine details of the flow field provided that adequate mathematical and numerical models are used. The viscosity and no-slip conditions on the surface of the body play a major role in the separation of the flow from smooth slender bodies. Hence inviscid approximations utilizing the potential flow assumption or based on the Euler equations

are inadequate. The Navier–Stokes equations are preferred in these cases. However, three-dimensional numerical simulations using the Navier–Stokes equations are still expensive in both CPU and memory requirements. The high computational cost required for the solution of the Navier–Stokes equations led to a search for simpler and more economical models of the flow field. Many existing viscous and incompressible computations use the steady boundary layer approximation to solve the flow field over a prolate spheroid of axial ratio 4:1[5,9,10] or 6:1.[11,12] The boundary layer equations are fully parabolic and therefore can be solved efficiently by marching from the front stagnation point. In regions of attached flow, or in regions with relatively slight circumferential reversed flow, good results were obtained by most boundary layer computations. However, numerical instabilities were detected near the location of the separation lines and no solutions could be obtained in separated flow regions. Williams[13] related these instabilities to the singular behaviour of the three-dimensional boundary layer equations near separation lines, which is similar to the singularity found in the two-dimensional boundary layer equations near a separation point. The appearance of numerical instabilities is usually interpreted as the onset of separation, but no reliable or physically accurate boundary layer solutions can be expected in these regions.

The reduced Navier–Stokes (RNS) and thin layer (TL) approximations occupy the middle ground between the Navier–Stokes equations and the boundary layer equations. In the RNS approximation the diffusion terms along the co-ordinate lines that approximately coincide with the mainstream direction are neglected. In the TL approximation the circumferential diffusion is neglected as well and only the diffusion normal to the body is retained. By neglecting the diffusion terms along the mainstream direction (and in the circumferential direction), the equations are simplified and may be solved more effiiciently. Rubin and Reddy[14] showed that the RNS equations contain all the important terms of the Navier–Stokes equations for high-Reynolds-number flows. Rosenfeld[15] proved for the incompressible case that the RNS system of equations is still elliptic but of reduced order. These approximations do not suffer from any mathematical or numerical singularities and yield solutions very similar to the solutions obtained from the complete Navier–Stokes equations.

The TL equations are very common in the calculation of compressible flow fields by time (or time-like) marching. As the Mach number decreases, the convergence rate often deteriorates. However, Pan and Pulliam[16] and Vatsa *et al.*[17] solved the compressible TL equations for the flow over a 6:1 spheroid at an incidence of 10° and a relatively low Mach number (Mach numbers of 0·029 and 0·4 were used in References 16 and 17 respectively). Although both works solve essentially the same problem by similar numerical methods, the results differ in several aspects. Only the skin friction and pressure distribution on the spheroid as well as the particle traces in a cross-flow plane were present.

In all these studies based on the TL equations the reduced ellipticity of the approximate differential equations is not utilized to save computational resources. The only saving in CPU time is obtained from the reduction in the number of algebraic operations resulting from a smaller number of viscous terms. This was noted by Rubin and Lin,[18] who suggested a solution method that takes advantage of the special form of the two-dimensional incompressible RNS equations. The momentum *and* continuity equations are solved as a coupled set of equations by an iterative marching procedure. No special treatment of the continuity equation is required as in the fractional step or artificial compressibility methods. Israeli and Lin[19] improved the convergence properties of the original method by modifying the discrete streamwise momentum equation such that upon convergence the modification vanishes. The method was extended by Rosenfeld[15] and Rosenfeld *et al.*[20] to the three-dimensional case using curvilinear orthogonal co-ordinate systems. This efficient solution method solves the RNS equations with an effort similar to that of solving

the boundary layer equations. However, the pressure is not imposed but interacts with the velocity field and thus the singularity of the boundary layer equations is removed.

In the present work a detailed simulation of the steady, incompressible and laminar flow field over a prolate spheroid of axial ratio 6:1 at an incidence of 10° and a Reynolds number of $1{\cdot}6 \times 10^6$ (based on the length of the spheroid) is presented. The numerical method of Rosenfeld[15] and Rosenfeld *et al.*[20,21] is used to solve the RNS approximation with primitive variables in an orthogonal co-ordinate system. The RNS approximation allows one to extend the boundary layer solution to vortical flow regions at a moderate computational cost. A relatively small number of mesh points are adequate to correctly resolve the flow field in the attached and longitudinal vortical flow regions owing to a careful selection of the location of the outer and downstream boundaries of the computational domain. The results allow the description of the flow field over substantial parts of the spheroid. Special emphasis is given to the investigation of the longitudinal vortical flow regions.

2. METHOD

2.1. Mathematical formulation

The reduced Navier–Stokes equations are written in a general axisymmetric curvilinear orthogonal co-ordinate system using primitive variables. The three orthogonal co-ordinates ρ, θ and ξ run approximately in the normal, circumferential and mainstream directions respectively. The mesh points are redistributed by one-dimensional stretching functions into another orthogonal co-ordinate system: q, s and t respectively.

The physical components of velocity along the co-ordinate lines are (V_q, V_s, V_t). In the present formulation the velocity is given in a scaled form (u, v, w) defined by

$$u = h_q V_q, \qquad v = h_s V_s, \qquad w = h_t V_t, \tag{1}$$

where h_q, h_s and h_t are the geometrical scale factors of the orthogonal co-ordinate system.

2.1.1. The governing equations. The continuity equation is given by

$$\frac{\partial(\sigma u)}{\partial q} + \frac{\partial(\tau v)}{\partial s} + \frac{\partial(\delta w)}{\partial t} = 0. \tag{2}$$

In an orthogonal co-ordinate system the mixed derivatives appearing in the laminar diffusion terms can be eliminated by using the continuity equation. The reduced Navier–Stokes momentum equations for the directions q, s and t respectively are given by[20]

$$\frac{1}{h_q}\left[\sigma u \frac{\partial}{\partial q}\left(\frac{u}{h_q}\right) + \tau v \frac{\partial}{\partial s}\left(\frac{u}{h_q}\right) + \delta w \frac{\partial}{\partial t}\left(\frac{u}{h_q}\right)\right] + \frac{1}{2}\left(\delta \frac{\partial \beta}{\partial q} v^2 + \sigma \frac{\partial \gamma}{\partial q} w^2 - \delta \frac{\partial \alpha}{\partial t} uv\right)$$
$$= -\sigma \frac{\partial P}{\partial q} + \frac{1}{Re}\left[\frac{\partial}{\partial q}\left(\alpha \frac{\partial}{\partial q}(\sigma u)\right) + \frac{1}{\delta}\frac{\partial^2 u}{\partial s^2} + \frac{\partial}{\partial q}\left(\frac{1}{\delta}\right)\frac{\partial v}{\partial s} - \frac{\partial}{\partial q}\left(\delta \frac{\partial \alpha}{\partial t} w\right)\right], \tag{3a}$$

$$\frac{1}{h_s}\left[\sigma u \frac{\partial}{\partial q}\left(\frac{v}{h_s}\right) + \tau v \frac{\partial}{\partial s}\left(\frac{v}{h_s}\right) + \delta w \frac{\partial}{\partial t}\left(\frac{v}{h_s}\right)\right] - \frac{1}{2}\left(\delta \frac{\partial \beta}{\partial t} vw + \sigma \frac{\partial \beta}{\partial q} uv\right)$$
$$= -\tau \frac{\partial P}{\partial s} + \frac{1}{Re}\left[\frac{\partial}{\partial q}\left(\frac{1}{\delta}\frac{\partial v}{\partial q}\right) + \tau\beta \frac{\partial^2 v}{\partial s^2} - \delta \frac{\partial \beta}{\partial t}\frac{\partial w}{\partial s} - \sigma \frac{\partial \beta}{\partial q}\frac{\partial u}{\partial s}\right], \tag{3b}$$

$$\frac{1}{h_t}\left[\sigma u\frac{\partial}{\partial q}\left(\frac{w}{h_t}\right)+\tau v\frac{\partial}{\partial s}\left(\frac{w}{h_t}\right)+\delta w\frac{\partial}{\partial t}\left(\frac{w}{h_t}\right)\right]+\frac{1}{2}\left(\delta\frac{\partial\beta}{\partial t}v^2+\delta\frac{\partial\alpha}{\partial t}u^2-\sigma\frac{\partial\gamma}{\partial q}uv\right)$$
$$=-\delta\frac{\partial P}{\partial t}+\frac{1}{Re}\left\{\frac{\partial}{\partial q}\left(\frac{1}{\tau}\frac{\partial w}{\partial q}\right)+\frac{1}{\sigma}\frac{\partial^2 w}{\partial s^2}+\frac{\partial}{\partial q}\left[\frac{\partial}{\partial t}\left(\frac{1}{\tau}\right)u\right]+\frac{\partial}{\partial t}\left(\frac{1}{\sigma}\right)\frac{\partial v}{\partial s}\right\}, \tag{3c}$$

where

$$\alpha=1/h_q^2, \qquad \beta=1/h_s^2, \qquad \gamma=1/h_t^2, \tag{4a}$$

$$\sigma=\alpha J, \qquad \tau=\beta J, \qquad \delta=\gamma J, \tag{4b}$$

with the Jacobian J given by

$$J=h_q h_s h_t. \tag{4c}$$

2.1.2. The computational domain and the boundary conditions. The analytic orthogonal prolate co-ordinate system has been employed for its simplicity. The mesh points have been redistributed to allow clustering of grid points in the boundary layer region. A uniform distribution of points is maintained in the circumferential direction. The upstream boundary is placed downstream of the forward stagnation point in a region where the boundary layer approximation can still be justified.

The flow separation at the rear part of the spheroid, which produces reversed flow in the mainstream direction with strong viscous–inviscid interaction, can be accurately computed only if the downstream boundary is moved far enough into the wake and the number of mesh points is increased appropriately. Moreover, calculation of the flow near the rear stagnation point increases the number of iterations required for convergence of the discrete equations. As a result the total requirement of computer resources becomes too high.

A possible way to overcome this difficulty is to place the downstream boundary ahead of the rear stagnation point. Obviously, this simplification does not allow the solution of the global separation region and the upstream influence of it cannot be accounted for. However, physical intuition suggests that the upstream influence of this separation is small for high-Reynolds-number flows over slender bodies at intermediate incidences. Numerous solutions of similar flows using the singular boundary layer approximation have yielded good agreement with experimental data in the attached flow regions, although they totally excluded the effect of both vortical and global separation regions. This fact supports the hypothesis of the present work that the upstream influence of globally separated regions is limited under the above conditions. It was decided to adopt this approach to permit an affordable numerical solution of the problem.

The RNS equations require three boundary conditions on all the boundaries, except at the downstream boundary where a single condition should be specified. At the upstream boundary the velocity is specified as

$$u=u_{up}, \qquad v=v_{up}, \qquad w=w_{up}, \tag{5a}$$

where the subscript 'up' stands for the upstream conditions. The normal and circumferential components of velocity are approximated from the potential solution, except at the surface of the spheroid where the velocity vanishes. The mainstream component w_{up} is approximated by a Kárman–Pohlhausen profile. The value of the displacement thickness at the upstream boundary is approximated from the solution of the integral boundary layer equations given by Stock.[22]

Three boundary conditions should be specified for the outer boundary. Assuming that this boundary is far enough from the body, the potential flow values are given to the streamwise and

circumferential velocity components and to the pressure:

$$v = v_{pot}, \qquad w = w_{pot}, \qquad P = P_{pot}. \tag{5b}$$

The outer boundary may be placed closer to the body than in the case where uniform velocity is specified. This enhances the efficiency of the method and requires fewer mesh points in the normal direction, at the expense of excluding the computation of strong viscous–inviscid interaction regions such as in regions of global separation. It should be noted that if the outer boundary is moved far away from the body, the RNS equations will correctly simulate the flow in these regions as well.

The normal velocity component u is not prescribed at the outer boundary. Therefore the displacement effect caused by the viscous boundary layer is not preimposed. This displacement effect can be used as a driving mechanism for a viscous–inviscid interaction algorithm. This possibility was not explored in this study.

A Neumann-type boundary condition is given for the pressure at the downstream boundary:

$$\frac{\partial P}{\partial t} = \left(\frac{\partial P}{\partial t}\right)_{pot}. \tag{5c}$$

On the body the no-slip and no-injection conditions are used:

$$u = v = w = 0. \tag{5d}$$

The computational domain included only half the flow field because the flow is symmetric at intermediate incidences. On the leeward and windward symmetry planes, symmetry conditions are specified.

2.2. Numerical method

Details of the numerical procedure for the solution of the three-dimensional incompressible RNS equations in a generalized orthogonal co-ordinate system as well as its validation and assessment are given by Rosenfeld and Israeli[21] and Rosenfeld *et al.*[20] Therefore the solution method will be only briefly reviewed here.

The set of RNS differential equations was discretized by finite differences over a special choice of staggered grid which can maintain second-order spatial accuracy by defining the location of the pressure in the same place as the mainstream component of the velocity.[20,21] First-order smoothing terms were added only to the cross-flow convection terms of the momentum equations to improve the stability properties of the scheme in regions of large cross-flow velocity. No smoothing terms were added to the continuity equation. The non-linear difference equations were linearized by a single Newton–Raphson iteration and solved iteratively using global iterations.

A single global iteration is performed by marching from the upstream boundary to the downstream boundary. In each step of the marching process the finite difference form of the coupled continuity and momentum equations in a computational cross-flow plane is solved simultaneously without any splitting errors. The simultaneous solution ensures that the discrete forms of the continuity and the two linearized cross-flow momentum equations are satisfied exactly *even when the iterative solution is not converged.* Global iterations are required to satisfy the discrete streamwise momentum equations, which include terms involving downstream values of the pressure (known only from the previous global iteration). A significant reduction in storage can be achieved because only a single three-dimensional field (the pressure) must be stored while the velocity is regenerated during the marching process.

2.3. Geometrical and numerical details

In the present paper the details of the calculated flow over a prolate spheroid of axial ratio 6:1 and 10° incidence at a Reynolds number of $1{\cdot}6 \times 10^6$ (based on the major axis) are presented. The normalized axial direction along the major axis is $Z = \cos\xi$, so that $Z = -1$ and $Z = 1$ correspond to the nose and rear end of the spheroid respectively. The upstream and downstream boundaries of the computational domain are located at $Z = -0{\cdot}95$ and $Z = 0{\cdot}76$ respectively. The outer boundary is located at $\rho = 0{\cdot}22$ whereas the spheroid itself is at $\rho = 0{\cdot}17$. Since the outer boundary is close to the spheroid, the hyperboloid $\xi = \text{constant}$ can be approximated by the plane $Z = \cos\xi$. Consequently, the results will be presented in a cross-flow plane $Z = \text{constant}$ rather than for the $\xi = \text{constant}$ hyperboloids.

The computational mesh consisted of $25 \times 25 \times 33$ points in the normal, circumferential and axial directions respectively. Grid points were clustered near the surface of the spheroid by a hyperbolic stretching function to properly resolve the flow near the body. The physical distance between two adjacent points near the outer boundary is eight times bigger than that between two adjacent points near the body.

The total number of mesh points is modest. Nevertheless, the resolution obtained is acceptable owing to the relative proximity of the outer boundary and the location of the downstream boundary on the rear end of the spheroid. Thin layer solutions use significantly more mesh points but for a much larger domain of computation.[16,17] Consequently, the resolution near the surface is comparable. However, this choice limits the present solution to regions with no globally separated flows.

The solution converged to an RMS error of 10^{-8} in less than 20 global iterations, which required about 2 h CPU time on an IBM 3081D computer and about 350 000 words of storage.

Rosenfeld *et al.*[20,23] assessed the accuracy of the results and their dependence on the various parameters, including the mesh size and the location of the boundaries. It has been shown that the present mesh domain of computation can correctly resolve the flow field in both the attached and vortical flow regions over a slender spheroid. In the present paper we rely on these previous validation tests and proceed to study the flow field.

3. SURFACE PROPERTIES

It is widely accepted that understanding of the flow over three-dimensional configurations is possible only by studying the entire three-dimensional flow field. However, surface properties such as skin friction lines, the boundary layer integral thickness or the pressure distribution on the body are still of interest. In particular, it is useful to know the relation (if any) between the features of the flow field near the surface and the three-dimensional separation phenomena. In the following subsections the calculated results of the surface properties are depicted.

3.1. Skin friction and skin friction lines

The normalized skin friction coefficient vector on the surface of the spheroid, $\mathbf{C}_f = (C_{f,\xi}, C_{f,\theta})$, is defined by

$$\mathbf{C}_f = \frac{\tau_w}{\frac{1}{2}\rho V_\infty^2}\sqrt{(Re)}, \tag{6}$$

where τ_w is the shear stress vector on the surface, ρ is the density and V_∞ is the undisturbed velocity upstream. Figure 1 gives the distribution of $\mathbf{C}_f$ on the spheroid. In the present domain of computation the longitudinal component of skin friction, $C_{f,\xi}$ is always positive, indicating no

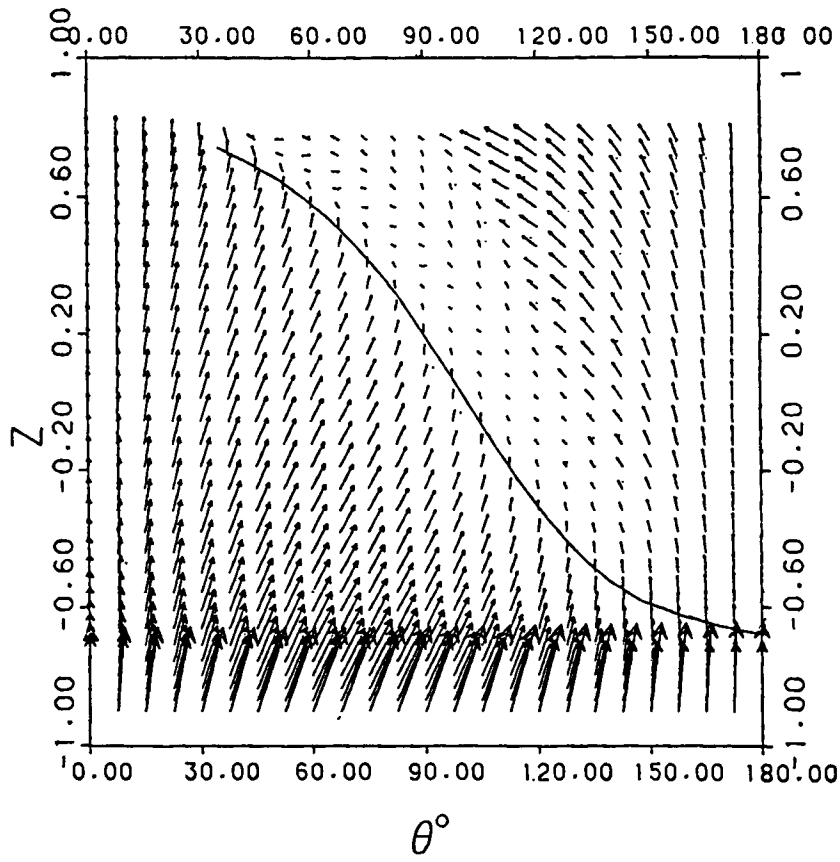

Figure 1. Distribution of the skin friction coefficient vector on the spheroid

reversal of the longitudinal flow near the surface of the spheroid. The circumferential component $C_{f,\theta}$ reverses its sign along an oblique line that emanates from the leeward symmetry plane near $Z=-0{\cdot}65$. This line will be called the zero-circumferential-skin-friction line (ZCFL).

Figure 2 compares the skin friction plot with the experimental results of Kreplin *et al.*[8] for the same case. In the laminar flow regions the agreement is usually good, bearing in mind the complexity of the flow field and the difficulties associated with measuring the skin friction in laminar regions.[8] The agreement at the upstream boundary near the leeward side is not as good. This is attributed to inaccurate upstream boundary conditions used for the circumferential velocity component.[20] The agreement improves at the downstream locations near the leeward symmetry boundary. The results are in disagreement at the downstream stations leeward of the ZCFL. It has been found experimentally that in this region the shear stress magnitude increases drastically because of the transition of the laminar flow into a turbulent flow. Vatsa *et al.*[17] obtained in their laminar flows calculations results similar to the present results. In the turbulent calculations they have found the solution to be sensitive to the assumed location of the transition to turbulence. Obviously, the present laminar simulation cannot reproduce the turbulent flow regions.

The contours of the *magnitude* of the normalized skin friction in the Z–θ plane are shown in Figure 3. The skin friction magnitude is large near the upstream boundary and generally

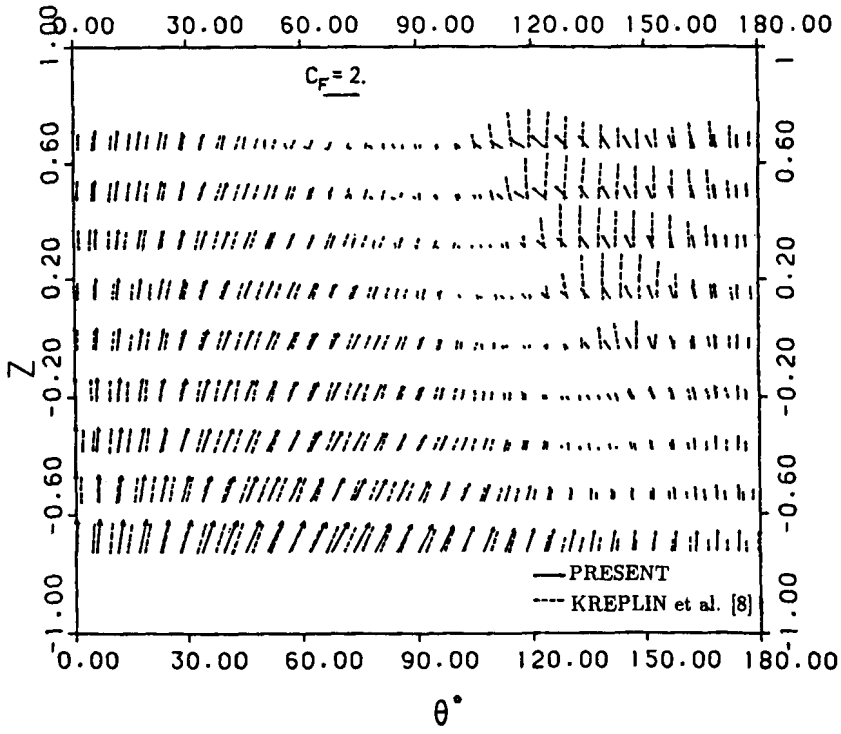

Figure 2. Comparison of the skin friction coefficient vector on the spheroid with experimental results

decreases in magnitude along the axial direction. However, at the leeward side near the downstream boundary the magnitude of the skin friction increases. The minimum in the magnitude of the skin friction is located on an oblique line on the surface (see Figure 3). It should be noted that the ZCFL and the minimal skin friction line do not coincide.

The skin friction lines are tangent to the shear stress vector on the surface of the body and can be computed by integration of

$$\frac{h_s \mathrm{d}s}{h_t \mathrm{d}t} = \frac{C_{f,s}}{C_{f,t}} = \frac{C_{f,\theta}}{C_{f,\xi}}. \tag{7}$$

In steady flows the skin friction lines are the projection of the limiting streamlines on the surface of the body. Hence the pattern of the skin friction lines may be indicative of the flow field in the vicinity of the body. Figure 4 shows the computed skin friction line pattern on the spheroid from two views. Near the upstream boundary and on most of the windward side the skin friction lines run generally in the direction of the outer potential flow. On the leeward side and near the downstream boundary the flow field is reversed in the circumferential direction. In the present domain of solution neither singular points (where the skin friction vanishes) nor closed convergence lines can be found. However, a long and swept convergence line can be clearly observed with skin friction lines merging into it from both sides. The precise origin of the convergence line cannot be defined and no singular points can be detected on the upstream part of the line. As pointed out by Dallmann,[7] it is impossible to determine uniquely from the surface flow whether the convergence line is also a separation line.

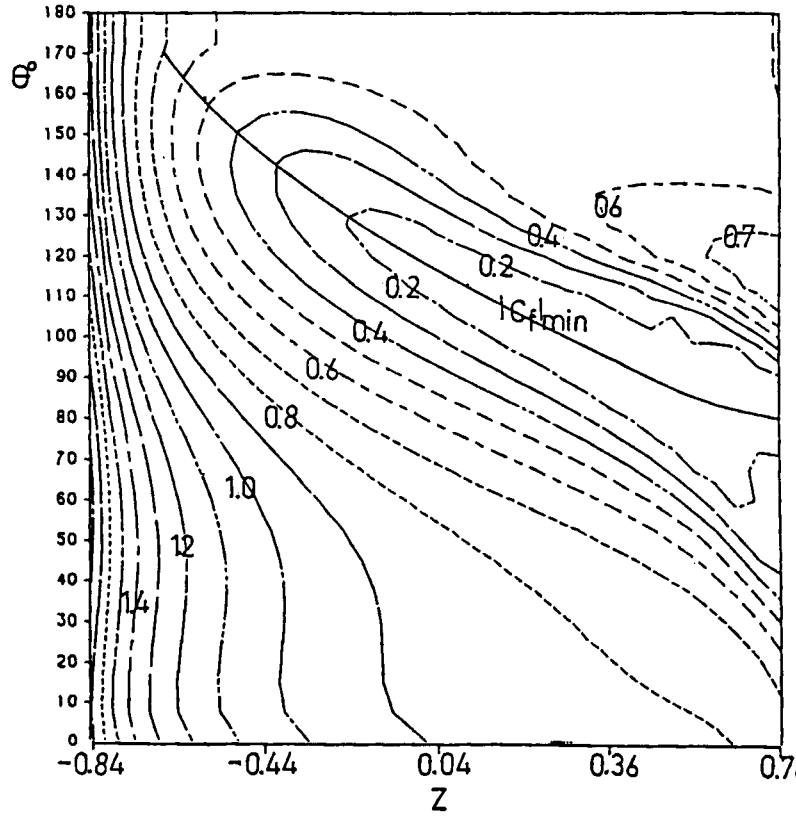

Figure 3. Contours of the skin friction coefficient magnitude

3.2. Pressure distribution on the spheroid

In the reduced Navier–Stokes equations the pressure is one of the dependent variables, in contrast to the boundary layer equations where the pressure is imposed from the outer potential solution. Therefore it is of interest to study the differences between the potential pressure and the computed pressure within the domain of solution. Unfortunately, no experimental data are available for comparison with the numerical results of the present case.

Figure 5 compares the computed (solid lines) and potential (dashed lines) isobars on the surface of the spheroid. A favourable longitudinal pressure gradient exists near the windward symmetry plane, while the pressure gradient at the leeward symmetry plane is adverse. In the circumferential direction the pressure decreases from the windward symmetry plane, reaches a minimal value and then increases towards the leeward symmetry plane. The minimal pressure lines of the computed and potential solutions are shown in Figure 5 as well. Near the upstream and windward boundaries no significant deviations can be detected. The discrepancy between the computed and potential pressure in the vicinity of the minimal pressure line and near the downstream boundary is substantial, indicating a strong viscous–inviscid interaction in these regions. This interaction increases the pressure at $90° > \theta > 30°$ in comparison with the potential pressure, thus contributing to the lift. The computed pressure field also reveals a property that does not appear in the potential solution. Near the downstream boundary at $\theta \approx 110°$ a second local minimum of the

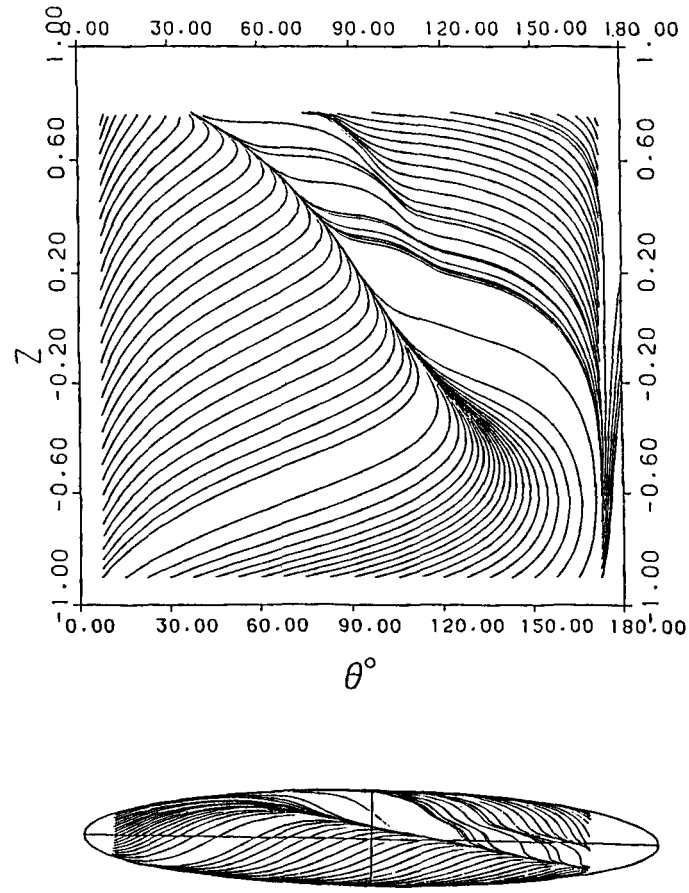

Figure 4. Skin friction lines (a) on the unwrapped spheroid and (b) on the spheroid

pressure can be observed. It will be shown in Section 4.3 that this minimum is related to the presence of a longitudinal vortex on top of this region.

3.3. The displacement velocity

A major effect of high-Reynolds-number boundary layer flows on the external inviscid flow is the displacement of the particle lines. In many two-dimensional interactive boundary layer computations the viscous effect is accounted for in the inviscid solution by replacing the zero-normal-velocity condition on a solid wall with a normal velocity specified from the viscous region calculation. In the present work we define for general three-dimensional cases a displacement velocity V_0 by

$$V_0 = (V_q - V_{q,\text{pot}})_{\text{outer}}, \tag{8}$$

where $V_{q,\text{pot}}$ is the potential value of the q-component of velocity and the subscript 'outer' stands for the value at the outer boundary. It should be noted that in the present simulation the component V_q at the outer boundary is not known *a priori* but is computed during the solution process.

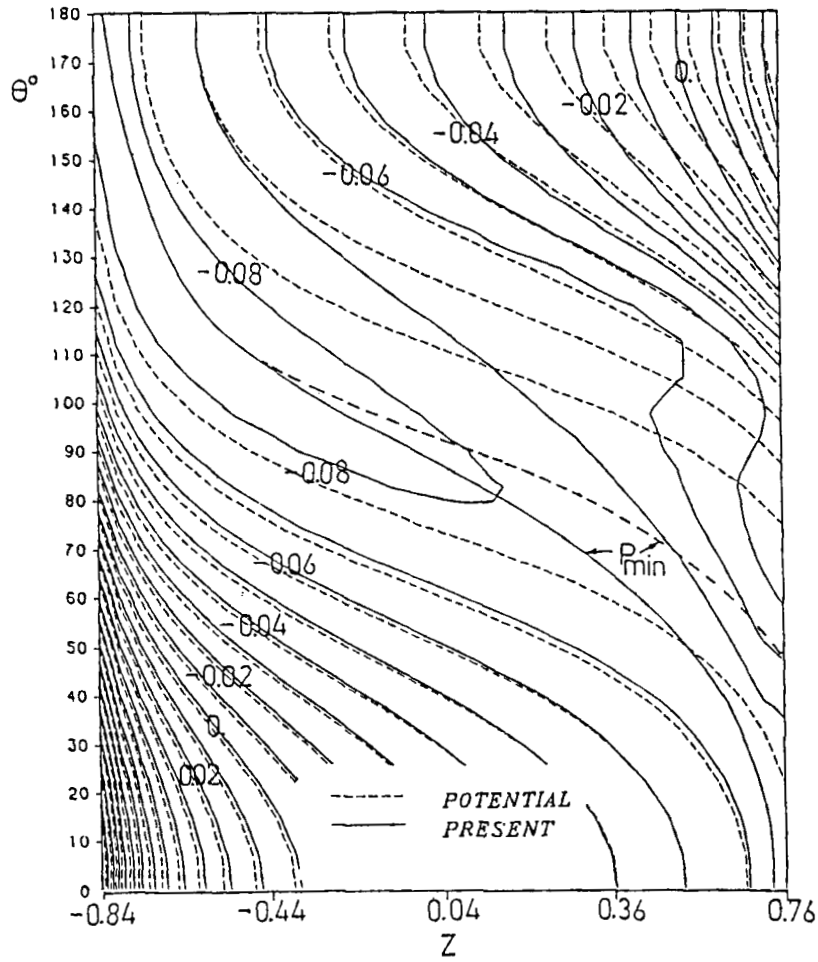

Figure 5. Contours of the computed and potential pressures on the spheroid

Figure 6 shows the displacement velocity contours. In large parts of the region the displacement velocity is positive but small in magnitude, as is usually found in thin attached boundary layer flows. Significant positive displacement velocity can be found near the downstream boundary for $60° < \theta < 90°$, presumably because of the thickening of the boundary layer near the global separation region. Significant *negative* displacement velocity is found on the leeward side. The region of negative displacement velocity extends into the windward side towards the downstream boundary, with an increase in its magnitude. The zero-displacement-velocity line, also shown in Figure 6, is slightly oblique, running windward for $Z > 0$.

4. THE THREE-DIMENSIONAL FLOW FIELD

Surface properties of flows over slender bodies are easy to relate to experiments. However, they can produce only a limited physical insight into the flow field and sometimes might even be misleading. It is essential to study the three-dimensional flow and to investigate its properties. In

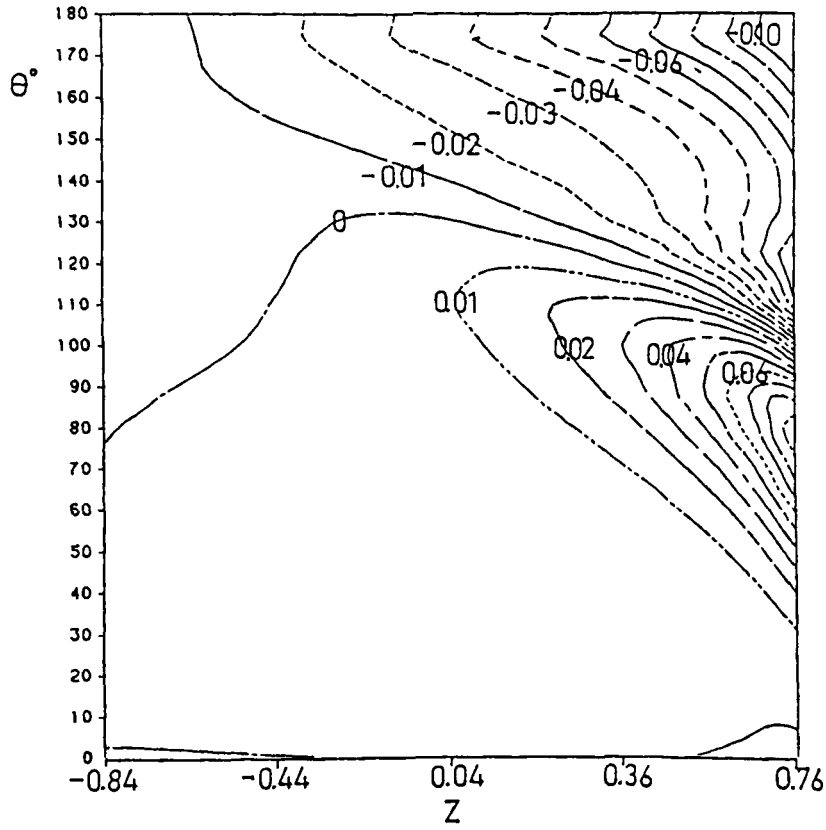

Figure 6. Contours of the displacement velocity on the spheroid

particular, the location and structure of the vortices can be studied only by considering the three-dimensional flow field.

4.1. Pressure field

Figure 7 presents a carpet plot of the computed (upper part) and potential (lower part) pressure fields at several cross-flow planes along the spheroid. The values $\rho = 0{\cdot}17$ and $0{\cdot}22$ correspond to the surface of the spheroid and to the outer boundary respectively. On the upstream cross-flow plane ($Z = -0{\cdot}44$) no significant difference can be found between the computed and potential pressure. At the next cross-flow plane ($Z = 0{\cdot}08$) some differences can be detected in a small region near the surface of the spheroid leeward of the minimum pressure (the computed pressure is larger than the potential pressure). At the next cross-flow planes the deviation of the computed pressure from the potential pressure not only increases but also spreads over a larger domain in the circumferential as well as the normal direction. In the downstream cross-flow planes a local second minimum in the computed pressure can be observed leeward of the minimum pressure. The local minimum extends into the normal direction but vanishes at the outer boundary where the potential pressure distribution is imposed. In the regions upstream of the global separation the outer boundary is placed far enough from the surface of the spheroid judging from the smooth blending of the computed pressure with the imposed potential pressure.

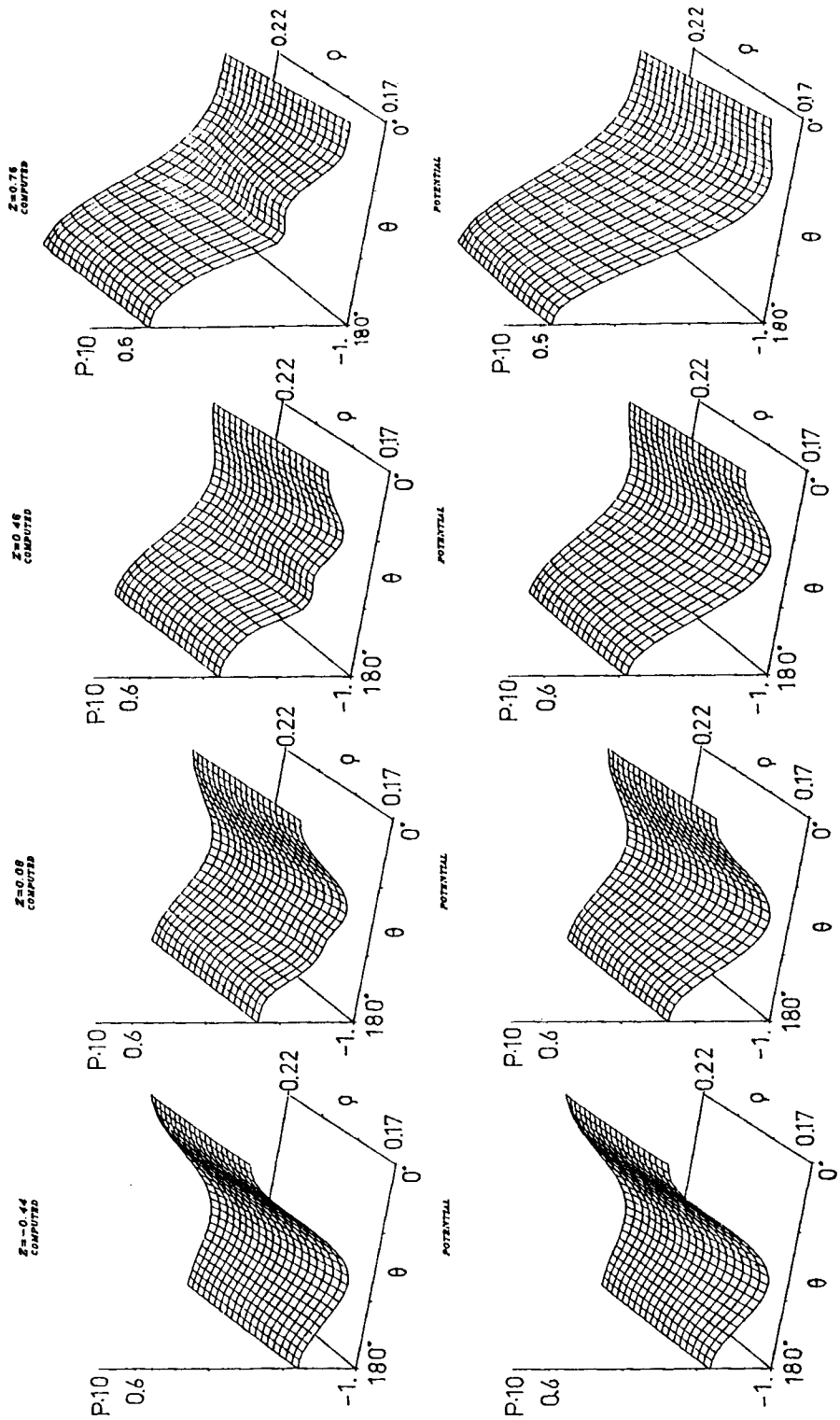

Figure 7. Comparison of the computed pressure with the potential pressure at several cross-flow sections

4.2. Velocity field

The next figures describe the velocity field. Figure 8 shows the projection of the velocity vector on several longitudinal planes (TETA is the value of θ). For the sake of clarity, only every second axial station is shown and the scale normal to the surface is five times larger than the longitudinal scale. Figure 9 shows the mainstream velocity component (V_t) profile along the normal direction η at several longitudinal planes and axial locations. The normalized co-ordinate η is defined by

$$\eta=(R-R_{\text{in}})\sqrt{\left(\frac{Re}{1+Z}\right)}, \tag{9a}$$

where R_{in} is the local radius of the spheroid and R is the radial distance from the axis of the spheroid given by

$$R=a\sinh\rho\sin\xi. \tag{9b}$$

The boundary layer of V_t is thin near the windward symmetry plane and at the front half of the body. Moreover, V_t is self-similar with respect to η at the windward symmetry plane and to some extent also at the leeward symmetry plane. A thick boundary layer of the velocity component V_t is found at $Z>0$ and $120°>\theta>60°$. This region coincides with the region where significant displacement velocity has been found (Figure 6). In the upstream part of that region the mainstream component of velocity is apparently close to being reversed since $\partial V_t/\partial q\to 0$. The longitudinal pressure gradient is adverse (see Figure 5), yet the velocity component V_t does not reverse its sign near the wall. On the contrary, the flow accelerates near the surface and a local maximum is formed. This local maximum disappears downstream and a thin boundary layer of V_t reappears in most of the downstream region of the computational domain. Because the phenomena are highly three-dimensional, two-dimensional reasoning fails completely in predicting the flow field in this region.

Figure 10 shows the projection of the velocity vector on several cross-flow planes. Here too the scale of the normal co-ordinate is enlarged five times and only every second circumferential point is plotted. ROIN is the value of R_{in} at the cross-section and R is the radial distance. Figure 11 describes the distribution of the circumferential velocity V_s with respect to η. In the windward part of the spheroid V_s exhibits a thin boundary layer behaviour, except far downstream where a circumferentially reversed flow exists. On the leeward side negative V_s can be found near the surface at all the cross-sections shown.

4.3. The vortical flow

Several interesting phenomena have been observed in the leeward and downstream parts of the spheroid, i.e. circumferentially reversed flow, convergence of the skin friction lines, significant deviation of the computed pressure from the potential pressure, negative displacement velocity and unusual velocity profiles. Apparently, a free vortex flow, which we shall refer to as a *longitudinal vortex*, might have been formed there. In compressible flows the longitudinal vortices can be identified from the density contours (or any another related quantity). Obviously, this procedure cannot be used in the present incompressible case.

In fact, even the terms 'free vortex' or 'longitudinal vortex' are ambiguous and a well accepted quantitative definition does not yet exist. Usually, the term 'vortex' is related to a global property of many particles rather than to a local property. A possible qualitative definition is: 'a vortex is a mass of fluid that rotates around a common axis'. In longitudinal vortex regions the particle traces spiral around a common axis which is also a particle line. Hence this vortex flow may be visualized by analysing the particle traces or a sequence of two-dimensional vector plots along the

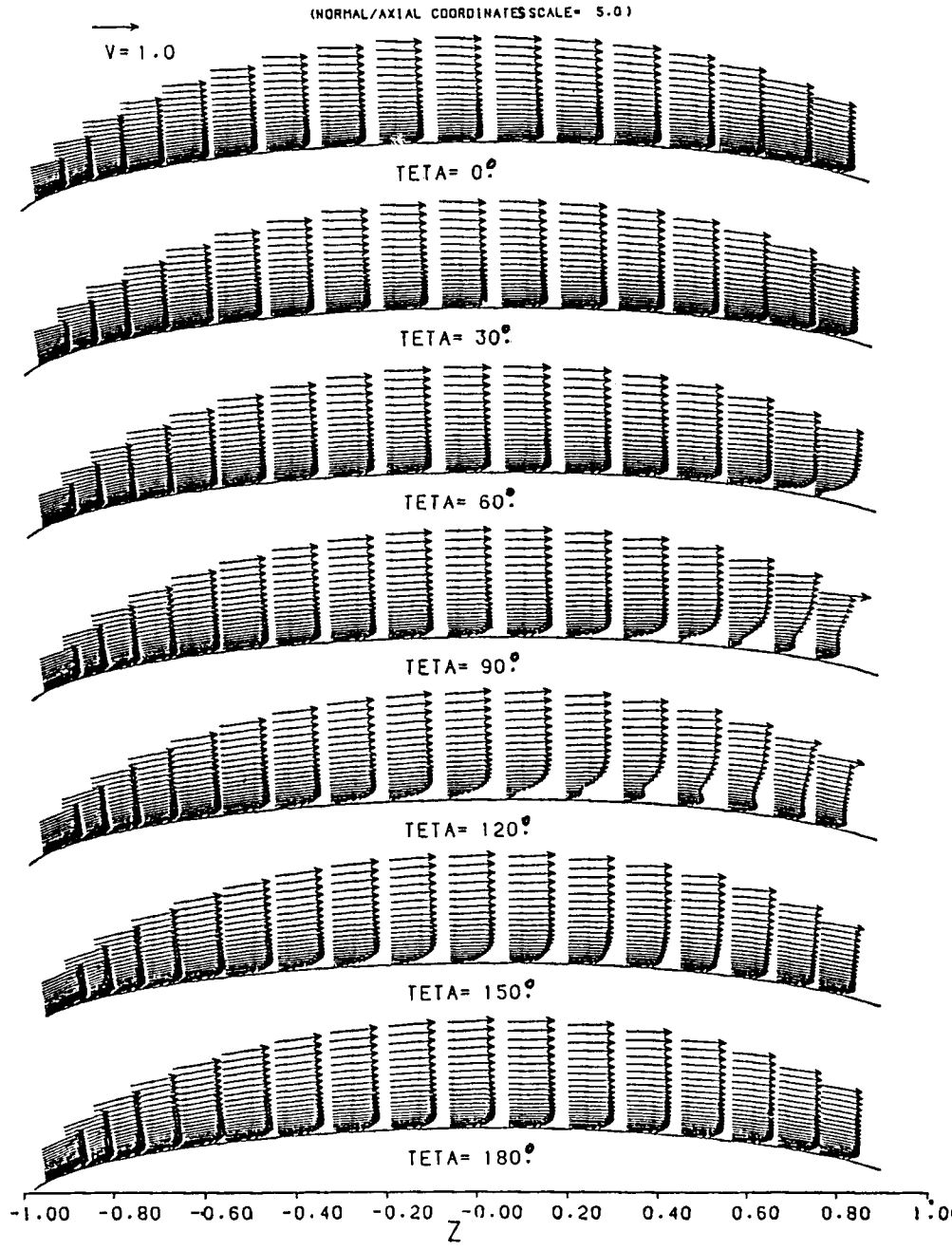

Figure 8. The velocity field in several longitudinal sections

body. In the present study we rely on the cross-flow velocity vector plots of Figure 10 to locate the vortical flow regions approximately.

The first sign of a possible vortical region can be observed at the cross-flow plane $Z=0{\cdot}08$ at $\theta \approx 132^\circ$ owing to the 'rotating' nature of the cross-flow. At $Z=0{\cdot}33$ and at $\theta \approx 140^\circ$ the vortical

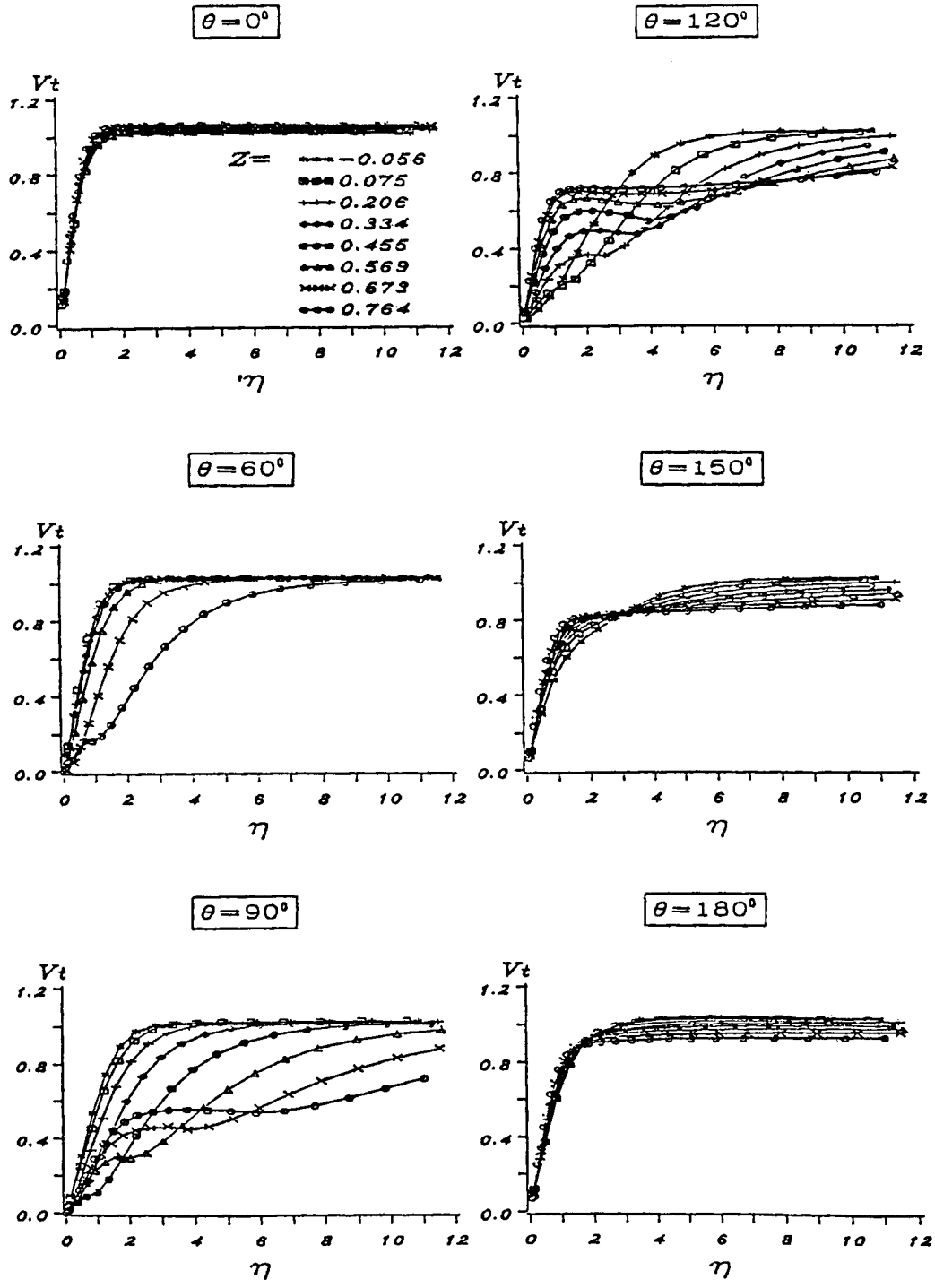

Figure 9. Distribution of the t-component of velocity

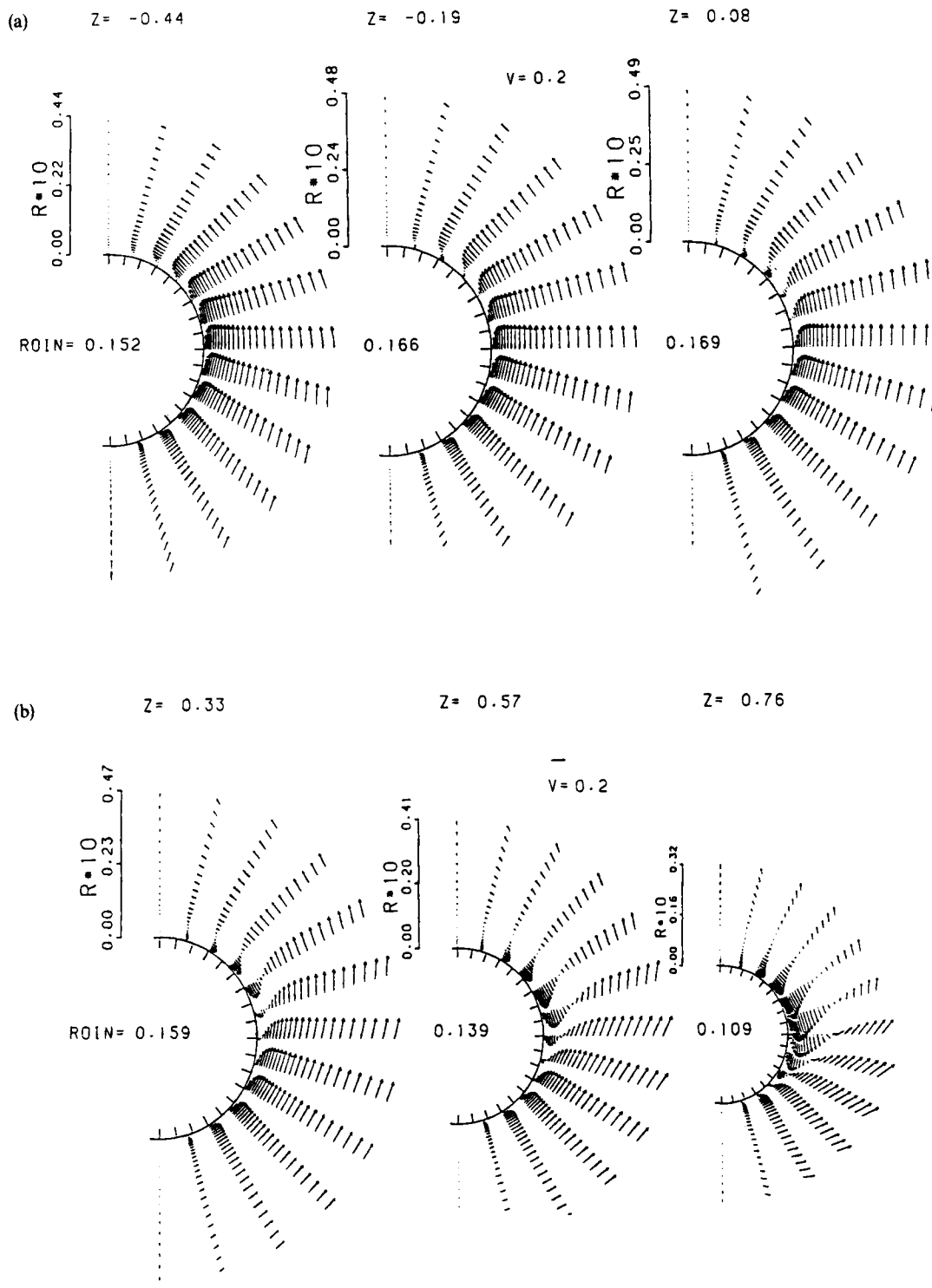

Figure 10. The velocity field in several cross-flow sections

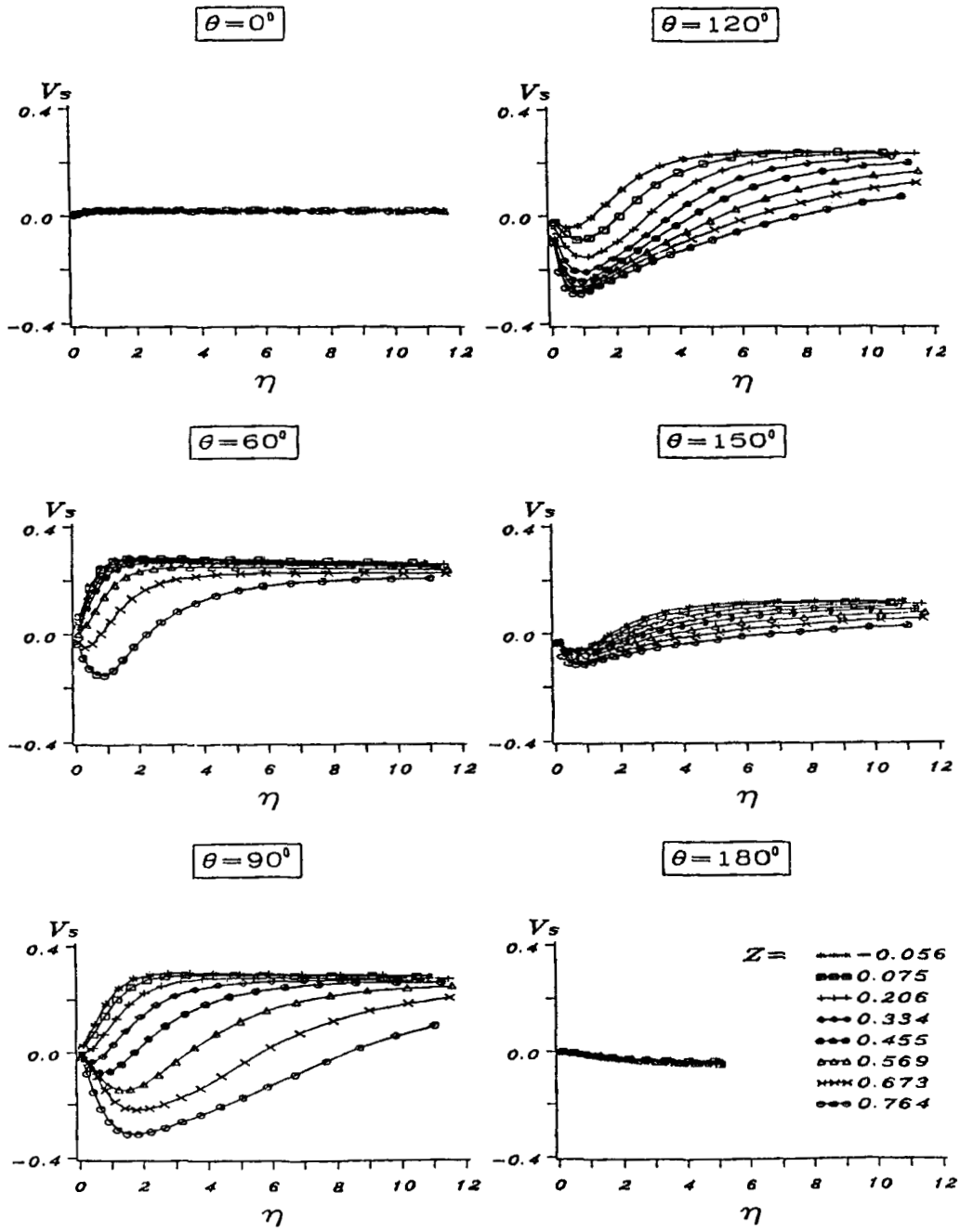

Figure 11. Distribution of the s-component of velocity

flow region is more prominent. The maximal magnitude of the circumferentially reversed flow is of the same order as the potential component. At the last two cross-flow planes shown, $Z=0{\cdot}57$ and $0{\cdot}76$, the vortical nature of the flow is even clearer. Regions of circumferentially reversed flow exist over major parts of the spheroid and the circumferential boundary layer is thick. Clearly, the

region of vortical flow spreads out in both the normal and circumferential directions. Figure 12 shows an expanded view of the cross-flow field at $Z=0{\cdot}57$. In this figure every circumferential point is plotted but some points near the outer boundary are omitted. The typical pattern of vortex flows can be observed, with the centre at $\theta \approx 115°$ and $\eta \approx 6$.

Since the axis of a vortex is also a particle line, the velocity component normal to it is zero. This property can be used to locate the axis of the longitudinal vortex by joining the points of zero cross-flow velocity. Obviously, this definition is exact only if the vortex centreline is perpendicular to the cross-flow plane. Nevertheless, in the case of slender bodies at intermediate angles of attack the deviation is usually small and this approximation yields acceptable results. Figure 13 shows two views of the approximate vortex centreline obtained by this method. The upper figure is an η–Z view while the lower figure is a θ–Z view. The vortex centre moves towards the windward side and away from the surface, yet the angle between the axial direction and the vortex centre is indeed small. The rate of departure of the vortex centreline from the body increases substantially, indicating a possible detachment of the vortex.

The presence of the longitudinal vortex has several effects on the properties of the flow field, both near the surface and away from it. The t-component of velocity shows a unique shape in the regions where the longitudinal vortex is embedded within the boundary layer (see Figures 8 and 9). In particular, an unexpected local maximum can be found near the surface. This shape of the t-

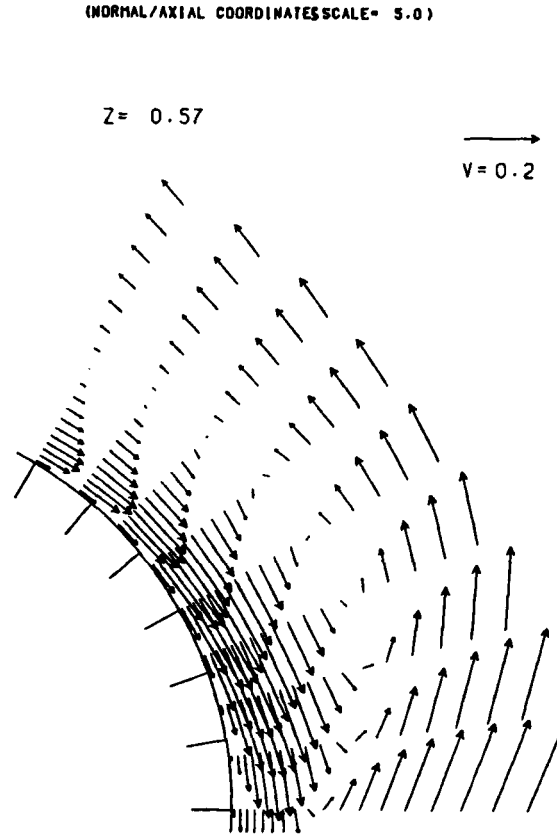

Figure 12. Enlargement of the velocity field at the cross-flow section $Z=0{\cdot}57$

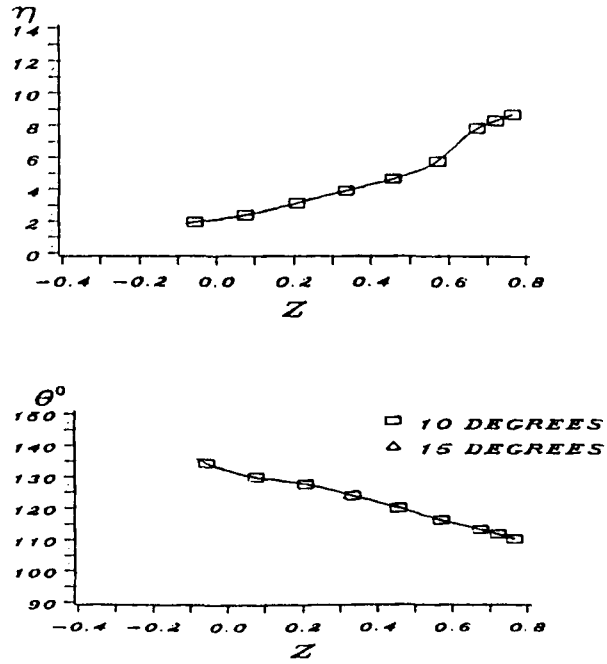

Figure 13. The vortex centreline

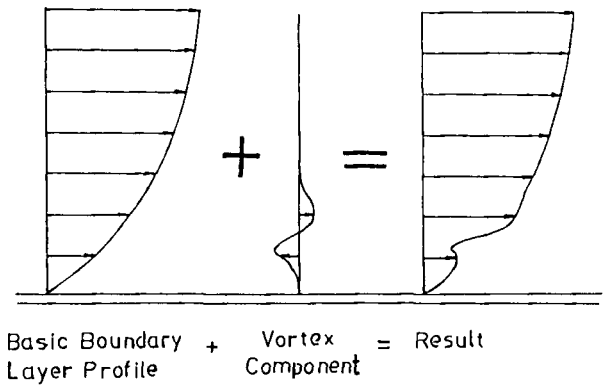

Figure 14. The formation of a local maximum in V_t

component of velocity is mainly a result of the projection of the three-dimensional flow field into a two-dimensional section. Owing to the inclination of the longitudinal vortex to the t-direction, the vortical flow has a component in the longitudinal direction as well (see Figure 14). The combination of a regular boundary layer velocity profile and the vortical flow velocity profile yields the local maximum of the t-component of velocity. It should be noted that the contribution of the vortical flow to the t-component of flow is significant only near the body, where the velocity due to the boundary layer is small. If the longitudinal vortex is far from the body, as is the case in

the downstream parts of the solution domain, the contribution of the vortical motion to V_t is negligible and V_t exhibits the regular monotonic velocity profile.

The negative displacement velocity near the leeward symmetry plane is another outcome of the longitudinal vortex, since it induces a negative normal velocity leeward of the vortex centreline. The local minimum of the pressure field (Figures 5 and 7) is yet another consequence of the vortex flow. However, the magnitude of the displacement velocity is small because of the weak strength of the longitudinal vortex.

4.4. Vorticity field

Many features of vortical flows are strongly related to the vorticity ω. It has been found in the present simulations that the q-component of vorticity is negligible and therefore its contribution will not be studied. Figure 15 shows the contours of the s- and t-components of vorticity at selected cross-flow planes. The horizontal axis is the circumferential co-ordinate θ and the vertical axis is the normal co-ordinate ρ. The values $\rho = 0{\cdot}17$ and $0{\cdot}22$ correspond to the surface of the spheroid and to the outer boundary respectively. Since the vorticity gradient near the surface of the spheroid is very large, contour lines are drawn only for $|\omega| < 100$ (non-dimensional).

The vorticity is generated at the solid wall and penetrates from the surface into the outer flow field by convection and diffusion. In most of the windward side the t-component of vorticity is negative while on the leeward side it is positive in the vicinity of the body. The location of the zero t-component of vorticity on the surface, $\omega_t = 0$, coincides with the location of the zero circumferential skin friction. Over large regions of the body the vorticity is confined to a thin boundary layer. The flow outside this region is essentially inviscid except in a domain where vorticity originating from the windward side penetrates into the outer flow. This region is small upstream but spreads out rapidly at the rear half of the spheroid. At the downstream boundary ($Z = 0{\cdot}76$) substantial vorticity exists even near the outer boundary, but it is confined to a narrow region in the circumferential direction, $60° < \theta < 120°$. It should be noted that the qualitative distribution of the t-component of vorticity in the cross-flow planes is similar to the vorticity distribution over a two-dimensional cylinder. The distribution of the s-component is qualitatively similar to the t-component except that no reversal in sign can be found.

The region of significant vorticity away from the body coincides with the region where a longitudinal vortex has been identified. The location of the vortex centre is shown in Figure 15 by the ' × ' symbols. No correlation could be found between the local absolute maximum of vorticity and the vortex centre except in the upstream parts of the vortex. The same findings are true in two-dimensional flows, i.e. the centres of the vortices behind a circular cylinder do not coincide with the extremum points of the vorticity field.

5. DISCUSSION

An indisputable definition of the three-dimensional separation line does not exist and probably no unique criterion can be found. Three-dimensional separation is usually a gradual process and therefore detection of the exact location of flow separation or detachment from a surface is difficult. A simple analysis by Lighthill[4] shows that the limiting streamlines leave a body rapidly near either a singular point ($|\mathbf{C}_f| \to 0$) or near a convergence line of the skin friction lines. Indeed, most researchers agree that in a separated flow region the limiting streamlines leave the surface 'rapidly'. Although this definition is conceptually clear, it is not a quantitative criterion. However, this reasoning is confined to the near-surface flow field, whereas three-dimensional separation is usually a global phenomenon that penetrates far out. As has already been mentioned, topological

analysis of the skin friction lines cannot uniquely determine whether the flow has been separated. The identification of separated flow regions should rely on the analysis of the entire three-dimensional flow.

A major feature of interest in the present work is the longitudinal vortices and their separation from the surface of the spheroid. In what follows, the term *separation* refers to the detachment of the longitudinal vortices *only*. The topic of flow separation is much broader (see e.g. References 2 and 6). However, because the present computational domain includes only regions with longitudinal vortical flows, no attempt will be made to discuss the full variety of flow separation types.

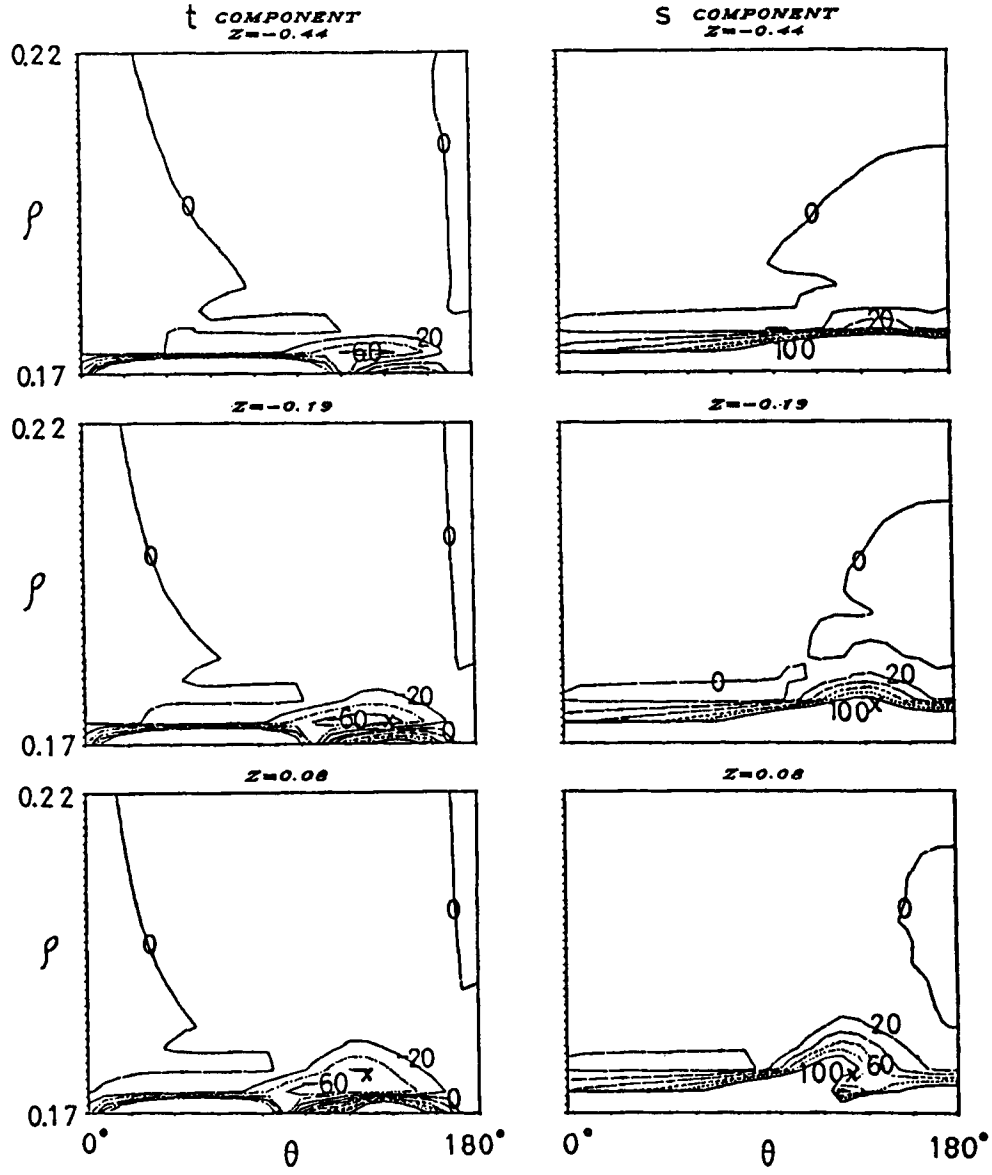

Figure 15. Contours of the t- and s-components of vorticity in several cross-flow sections

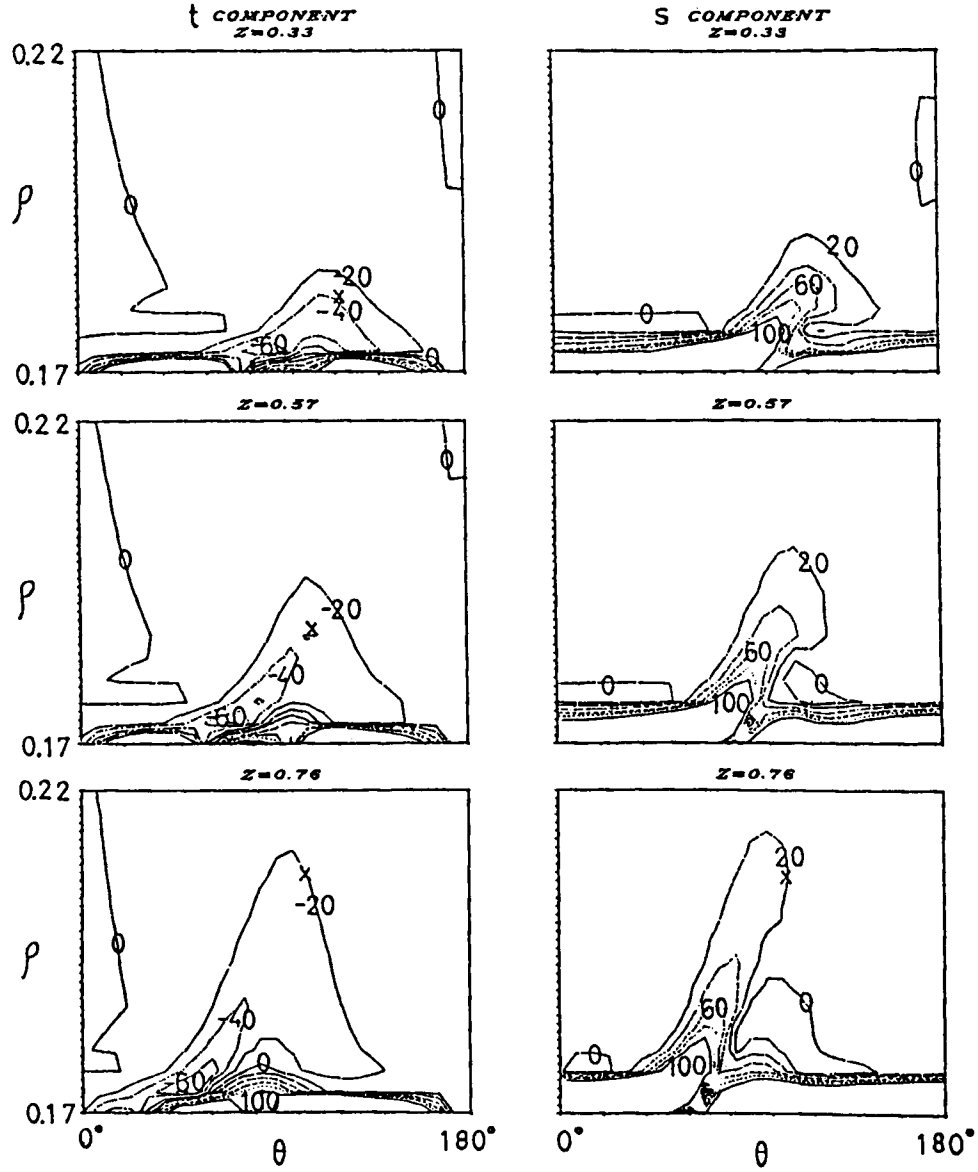

Figure 15. (Continued)

We suggest a somewhat narrow definition of flow separation: a vortical flow is separated if the distance of the vortex centreline from the body is 'large', i.e. when the centreline is outside the boundary layer region. Figure 13 reveals that the departure rate of the vortex centreline from the spheroid increases significantly at $Z \approx 0{\cdot}5$, where the vortex centre is at $\eta \approx 5$. (Near the downstream direction the rate decreases, presumably because of the effect of the downstream computational boundary.) This region coincides approximately with the disappearance of the local maximum of V_t near the spheroid. As may be recalled, this local maximum has been attributed to the presence of a vortex flow inside the boundary layer region. On the basis of these data it is

reasonable to assume that the longitudinal vortex separates near $Z=0{\cdot}5$. The vorticity distribution (Figure 15) confirms this observation, since the vorticity penetrates substantially outside the boundary layer in about that region.

Another possibility of defining the detachment of longitudinal vortices may be based on the value of the negative displacement velocity. When it exceeds a certain amount, the vortical flow may be considered detached. How that amount can be determined is not clear yet and additional study is required to evaluate this suggestion. Chapman[6] suggests a similar definition to locate the separation point at each cross-flow plane: 'the point where the local displacement thickness is a given amount larger than the average displacement thickness in the circumferential direction'.

Having established the existence of a detached vortex flow, we return to the examination of the flow properties near the surface. Figure 16 summarizes several characteristic lines on the surface of the spheroid that have been defined in the present paper. The lines shown are the zero-circumferential-friction line (ZCFL), the minimal skin friction line, the skin friction convergence line, the zero-displacement-velocity line, the minimal pressure line and the projection of the vortex centreline on the body.

It is worth noting that all the lines have similar shape although no two of them coincide. The zero-circumferential-skin-friction line lies leeward (about 15°) of the minimal pressure line and quite close to the skin friction convergence line, which in turn is about 4° leeward of the ZCFL. This is yet more computational evidence that the ZCFL does not generally coincide with the skin friction convergence line (see e.g. Reference 5). Reversed flow in the circumferential direction can be found near the spheroid as far upstream as $Z=-0{\cdot}65$, whereas a clear skin friction convergence line appears only at $Z\approx 0$. The skin friction convergence line should be the separation line

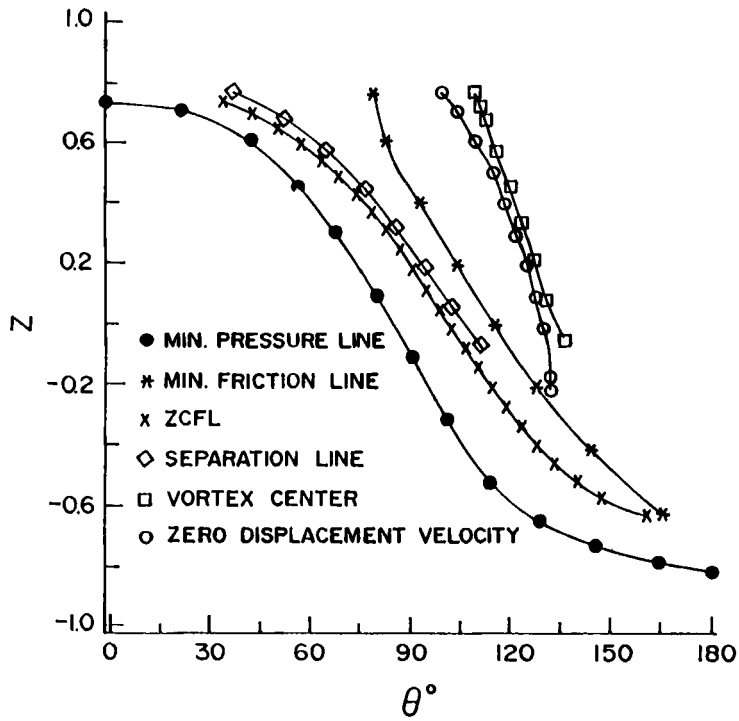

Figure 16. Summary of several characteristic lines on the spheroid

from which a separation surface emanates and rolls up into the vortical flow. However, although a clear convergence line is already formed at $Z \approx 0$, the three-dimensional field analysis has shown that the vortical flow is still embedded inside the boundary layer as far as $Z = 0{\cdot}5$. This is a computational manifestation of the generally accepted observation that convergence of the skin friction lines is not a sufficient condition for the detachment of the longitudinal vortices.[2] Note that the separation line is topologically indistinguishable from other skin friction lines since no singular points have been detected on it.

The shape of the lines reveals the strong three-dimensional effects near the separation line. The minimal skin friction line is at quite a distance leeward of the zero-circumferential-friction line and leeward of the separation line. Clearly, it cannot be used as an approximation of the separation line. The zero-displacement-velocity line and the projection of the vortex centreline are leeward of the separation line and close to one another, since the sign of the displacement velocity is closely related to the direction of the cross-flow velocity. The present study suggests that the zero-displacement-velocity line may give a better estimate of the vortex centreline projection on the body. Further study is required to establish the relationship between them.

In many two-dimensional viscous–inviscid interaction models the interaction algorithm is driven by an injection velocity computed from the viscous solution. In these cases the flow separation is described by a positive injection velocity. The three-dimensional extension of this algorithm can be based on the 'displacement velocity' concept that has been used in the present work. However, Figure 6 reveals that in the three-dimensional case vortical flow separation is not necessarily related to a positive injection velocity but to a combination of both positive and negative displacement velocities. Hence certain separation control devices or longitudinal vortex generators should use a combination of suction and injection. Devices based on the suction of the boundary layer may not work or may cause unexpected results in three-dimensional cases.

6. CONCLUDING REMARKS

The purpose of the paper has been to simulate numerically the *longitudinal vortical flow field* regions over a slender prolate spheroid at intermediate incidence using the reduced Navier–Stokes equations. The present work moves one step beyond the boundary layer approximation by relaxing the requirement of an imposed pressure field. The physical parameters were chosen so that no pronounced effects of the rear-end global separation are expected in the upstream vortical flow. Thus the solution of a domain that does not include the rear end of the spheroid is justified.

The main features of vortical laminar flow fields over blunt bodies at intermediate incidence have been successfully simulated. The quality of the results permitted a study of the laminar flow over a 6:1 spheroid at 10° incidence and shed some light on the structure of the highly three-dimensional flow field in the longitudinal vortex region. The vortical flow is relatively weak and has less pronounced effects than its counterpart flow over delta wings with sharp leading edges. It emanates from an oblique separation line to which the skin friction lines converge from both sides, but a clear vortex flow is observed only at the downstream part of the separation line. The origin of the separation line cannot be tracked and no primary singular points have been found on the upstream part of that line.

Comparison of the results with experiments suggests that an accurate simulation of the vortex flow requires the solution of the mixed laminar, turbulent and transitional flows. However, the analysis tools that have been developed and the qualitative flow properties deduced in the present study are believed to apply to the turbulent regimes as well.

REFERENCES

1. T. Y. Han and V. C. Patel, 'Flow separation on a spheroid at incidence', *J. Fluid Mech.*, **92**, 643–657 (1979).
2. M. Tobak and D. J. Peake, 'Topology of three-dimensional separated flows', *Ann. Rev. Fluid Mech.*, **14**, 61–85 (1982).
3. K. C. Wang, 'On the dispute about open separation', *AIAA Paper 83-0296*, 1983.
4. M. J. Lighthill, 'Attachment and separation in three-dimensional flow', L. Rosenhead (ed.), *Laminar Boundary Layers, Vol. II*, Oxford University Press, London, 1963, p. 72.
5. K. C. Wang, 'Boundary layer over a blunt body at low incidence with circumferential reversed flow', *J. Fluid Mech.*, **72**, 49–65 (1975).
6. G. T. Chapman, 'Topological classification of flow separation in three dimensional bodies', *AIAA Paper 86-0485*, 1986.
7. U. Dallmann, 'Topological structures of three-dimensional vortex flow separation', *AIAA Paper 83-1735*, 1983.
8. H. P. Kreplin, H. Vollmers and H. U. Meier, 'Measurements of the wall shear stress on an inclined prolate spheroid', *Z. Flugwiss. Weltraumforsch*, **6**, 248–252 (1982).
9. T. Cebeci, A. A. Khattab and K. Stewartson, 'Three-dimensional laminar boundary layers and the Ok of accessibility', *J. Fluid Mech.*, **107**, 57–87 (1981).
10. V. C. Patel and D. H. Choi, 'Calculation of three-dimensional laminar and turbulent boundary layers on bodies of revolution at incidence', in L. J. S. Bradbury, F. Durst, B. E. Launder, F. W. Schmidt and J. H. Whitelaw (eds.), *Turbulent Shear Flows II*, Springer, New York, 1980, p. 199.
11. W. Schönauer and K. Häfele, 'Experience with the numerical solution of the 3-D laminar boundary layer equations in streamline coordinates', *Comput. Fluids*, **15**, 93–118 (1987).
12. V. C. Patel and J. H. Baek, 'Boundary layers and separation on a spheroid at incidence', *AIAA J.*, **23**, 55–63 (1985).
13. J. C. Williams, 'Singularities in solutions of the three-dimensional laminar boundary layer equations', *J. Fluid Mech.*, **160**, 257–279 (1985).
14. S. G. Rubin and D. R. Reddy, 'Analysis of global pressure relaxation for flows with strong interaction and separation', *Comput. Fluids*, **11**, 325–339 (1983).
15. M. Rosenfeld, 'Numerical solution of the viscous and incompressible flow around a slender body at incidence', *Ph.D. Thesis*, Technion—Israel Institute of Technology, 1986.
16. D. Pan and T. H. Pulliam, 'The computation of steady 3-D separated flows over aerodynamic bodies at incidence and yaw', *AIAA Paper 86-0109*, 1986.
17. V. N. Vatsa, J. L. Thomas and B. W. Wedan, 'Navier–Stokes computation of prolate spheroids at angle of attack', *AIAA Paper 87-2627*, 1987.
18. S. G. Rubin and A. Lin, 'Marching with the parabolized Navier–Stokes equations', *Isr. J. Technol.*, **18**, 21–31 (1980).
19. M. Israeli and A. Lin, 'Marching iterative methods and boundary conditions for the parabolized Navier–Stokes equations', *Comput. Fluids*, **13**, 397–409 (1985).
20. M. Rosenfeld, M. Israeli and M. Wolfshtein 'A method for solving three-dimensional viscous incompressible flows over slender bodies' *J. Comput. Phys.*, **88**, 255–283 (1990).
21. M. Rosenfeld and M. Israeli, 'Numerical solution of incompressible flows by a marching multigrid nonlinear method', *AIAA J.*, **25**, 641–647 (1987).
22. H. W. Stock, 'Laminar boundary layers on inclined ellipsoids of revolution', *Z. Flugwiss. Weltraumforsch*, **4**, 217–224 (1980).
23. M. Rosenfeld, M. Israeli and M. Wolfshtein, 'A numerical study of the skin friction on a spheroid at incidence', *AIAA J.*, **26**, 129–136 (1988).